Electron-impact excitation of Xe^{26+} and its resultant spectral signature

N R Badnell[1], K A Berrington[2], H P Summers[1], M G O'Mullane[1], A D Whiteford[1] and C P Ballance[3]

[1] Department of Physics, University of Strathclyde, Glasgow, G4 0NG, UK
[2] School of Science and Mathematics, Sheffield Hallam University, Sheffield, S1 1WB, UK
[3] Department of Physics, Rollins College, Winter Park, FL 32789, USA

Abstract

We have carried out a 129 close-coupling level Dirac–Coulomb R-matrix calculation for the electron-impact excitation of Ni-like Xe. We have utilized this data to generate the spectral signature of Xe^{26+} in terms of feature photon-emissivity coefficients ($\mathcal{F}\text{-}\mathcal{PEC}$s). We have compared these $\mathcal{F}\text{-}\mathcal{PEC}$s with those generated using semi-relativistic plane-wave Born excitation data, which forms the heavy species baseline for the Atomic Data and Analysis Structure (ADAS). We find that the Born-based $\mathcal{F}\text{-}\mathcal{PEC}$s give a reasonable qualitative description of the spectral signature but that, quantitatively, the R-matrix-based $\mathcal{F}\text{-}\mathcal{PEC}$s differ by up to a factor of 2. The spectral signature of heavy species is key to diagnosing hot plasmas such as will be found in the International Thermonuclear Experimental Reactor.

1. Introduction

The spectral signature of heavy species, elements heavier than zinc, say, is a key issue for the diagnostic modelling of the hot plasmas expected to be found in the international plasma burning experiment (ITER Physics Basis 1999), on ITER (International Thermonuclear Experimental Reactor)—the traditional 'astrophysical' light–medium-weight elements being fully stripped at the temperature regimes of interest. Furthermore, heavy species are actively under study within the context of microlithographic light sources so as to provide the next generation of etching for the semiconductor industry (Smith 2004). Of course, Ni-like ions themselves have been of particular interest ever since x-ray lasing was first observed (MacGowan *et al* 1987).

The spectral modelling of heavy species is different from the traditional individual line analysis of light astrophysical species. The complex atomic structure of heavy species gives rise to millions of lines and hence a grass-like structure to the emission spectrum, which defies individual line analysis. What one is looking to model is an envelope of lines—a feature—and

to treat a feature analogously to a line. The envelope may be defined simply by the resolution of the spectrometer. In a plasma of many emitting stages and/or elements one seeks to identify a 'fingerprint' feature which is characteristic and composed of a single or, perhaps, several adjacent ionization stages of an element.

Modelling even a few stages of a heavy species requires a vast amount of atomic data, which cannot be provided in general from state-of-the-art collision codes such as R-matrix (Berrington *et al* 1995). Instead, rather simple but comprehensive methods must be used to assemble a baseline of data. Within the Atomic Data and Analysis Structure (ADAS) (Summers 2003) Cowan's structure code (Cowan 1981) and the AUTOSTRUCTURE code (Badnell 1987, 1997) provide semi-relativistic energy levels, radiative rates and plane-wave Born electron-impact excitation collision strengths. Such simple collision data cannot hope to model individual lines as accurately as R-matrix data but, as we have already noted, spectroscopic modelling takes place with an assembly of lines (the feature) and the summation over many lines means that the errors in the individual lines tend to cancel statistically. The validity of such an approach is borne out by a comparison of the measured and baseline theoretical emission spectra from W^{38+} through W^{48+} (Pütterich *et al* 2004). The baseline approach can also be used as a first cut to identify key stages and levels which warrant a more precise, individualized, investigation. It is this philosophy which we seek to support and address within this paper. Of course, the Ni-like stage is a relatively simple one for a heavy species but it is an example of a diagnostically significant stage which emits identifiable lines and for which higher quality atomic data can be easily incorporated into the feature-type analysis. Nevertheless, it is still a computationally demanding stage for state-of-the-art collision calculations.

Here, we report on results for feature photon-emissivity coefficients ($\mathcal{F}$-$\mathcal{PEC}$s) for Ni-like Xe^{26+}. We first carried out an ionization balance calculation for the Xe isonuclear sequence so as to identify the temperature range of peak abundance for the Ni-like stage. The totality of spectral emission from this and surrounding stages was determined using the baseline atomic data and features identified within the $\lambda = 10$–20 Å range for Xe^{26+}. The experiment was then made of replacing the plane-wave Born collisional data with that from a 129 close-coupling (CC) level Dirac–Coulomb R-matrix calculation, and which we report on here, to see the effect this had on the feature.

Our Dirac–Coulomb R-matrix calculation itself features a novel approach, viz we utilize the existing Dirac atomic R-matrix code (DARC) (Ait-Tahar *et al* 1996) to set up the $(N + 1)$-electron Hamiltonian and have then interfaced this with our existing parallel diagonalization code and our parallel outer region code (Mitnik *et al* 2003), along with straightforward modifications to the latter two codes to handle relativistic wavefunctions from the inner region and the jj-coupling scheme (as opposed to the jK-coupling scheme utilized for Breit–Pauli calculations).

The remainder of this paper is organized as follows. In the next section we discuss our theoretical approach to the relativistic R-matrix collision problem and its implementation codewise. In section 3 we describe the details of our atomic structure calculation for Xe^{26+}. In section 4 we discuss the details of our R-matrix calculation, and present some illustrative results. In section 5 we discuss some of the theory behind the modelling of the feature photon-emissivity coefficient and present our results. Finally, we conclude in section 6 with a summary of our findings.

2. Theory and codes

With a nuclear charge of $Z = 54$, we seek a fully relativistic solution for the atomic structure and collision problem. We use a multi-configuration Dirac–Fock (MCDF) approach to set up
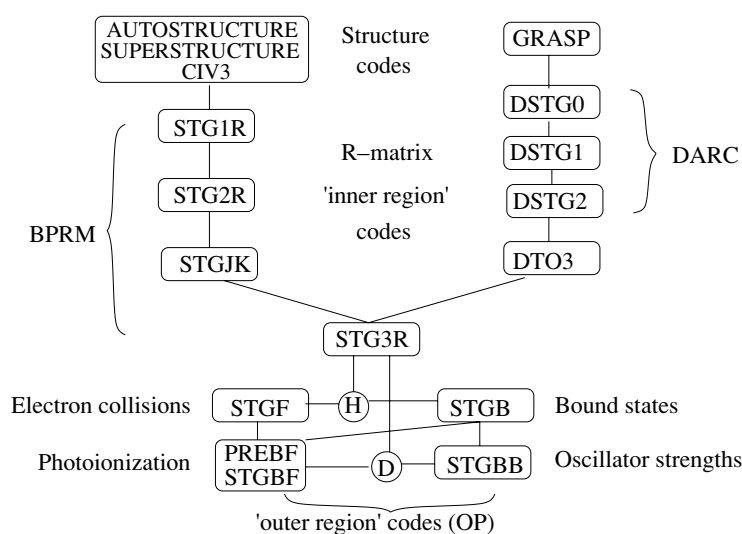
AUTOSTRUCTURE SUPERSTRUCTURE CIV3 — Structure codes — GRASP

STG1R — R–matrix 'inner region' codes — DSTG0

STG2R — DSTG1

STGJK — DSTG2

BPRM — DARC

DTO3

STG3R

Electron collisions — STGF —(H)— STGB — Bound states

Photoionization — PREBF STGBF —(D)— STGBB — Oscillator strengths

'outer region' codes (OP)

Figure 1. Flow diagram illustrating the interconnectivity between the Breit–Pauli, Dirac–Coulomb and Opacity Project (OP) R-matrix code suites.

a target prior to the collision calculation, as implemented by the general relativistic atomic structure package (GRASP) (Grant *et al* 1980), specifically the GRASP^0 code (Norrington 2004).

Our choice of collision approach is based upon our subsequent modelling methodology. Specifically, we work at plasma densities such that the time between collisions is long compared to that of the lifetime of autoionizing levels (Summers 1994) and so these levels do not need to be included explicitly within the generalized collisional-radiative (GCR) population rate equations. Rather, they can be included implicitly as resonances within the collision rates. The R-matrix method (Burke and Robb 1975) is ideally suited to this approach.

The Dirac atomic R-matrix code (DARC) (Ait-Tahar *et al* 1996, Norrington 2004) provides such an R-matrix solution to the collision problem based upon the Dirac–Coulomb Hamiltonian. However, much effort has gone into developing R-matrix codes based upon LS-coupling and Breit–Pauli Hamiltonians (Berrington *et al* 1995), in particular, for parallelization (Mitnik *et al* 2003, Ballance and Griffin 2004) and photon processes (Berrington *et al* 1987, Robicheaux *et al* 1995). The code structure and nature of the physics problem means that we can easily adapt these developments for use with the Dirac–Coulomb R-matrix method.

Specifically, the main computational effort in determining the R-matrix solution within the inner region lies in the diagonalization of the $(N+1)$-electron Hamiltonian. Common to all R-matrix computer packages, this diagonalization takes place in a standalone 'stage'. There is nothing fundamentally specific to DARC about the DSTG3 DARC diagonalization stage. (One must recognize and handle the fact that the zero-order basis solutions are resolved by $\kappa = l, -l - 1$ now, rather than just l, where l is the orbital angular momentum.) Thus, we have written an interface code (DTO3) which converts the Hamiltonian and dipole matrices constructed by DARC DSTG2 to the RECUPH.DAT and RECUPD.DAT file formats utilized by the Breit–Pauli originated STG3R code. This (RECUPH.DAT) enables us to use the scaLAPACK-based parallel diagonalization code PSTG3R (Mitnik *et al* 2003) and naturally leads on to an outer-region solution based upon the suite of codes originally developed for the Opacity Project (see Berrington *et al* (1987)), e.g., STGF (and its parallel version PSTGF and radiation damped versions P/STGFDAMP) for electron-impact excitation, and STGB, STGBF, STGBB, STGBF0DAMP etc for

Table 1. Level energies (Ry) for Xe^{26+}.

Index	Configuration	Symmetry	MCDF[a]	Observed[b]
1	$3d^{10}$	$^1S_0$	−0.100	
2	$3d^94s$	$^3D_3$	43.368	
3	$3d^94s$	$^1D_2$	43.446	43.475
4	$3d^94s$	$^3D_1$	44.381	
5	$3d^94s$	$^3D_2$	44.441	44.448
6	$3d^94p$	$^3P_2$	47.261	
7	$3d^94p$	$^1F_3$	47.322	
8	$3d^94p$	$^3F_2$	48.282	
9	$3d^94p$	$^3P_1$	48.400	48.405
10	$3d^94p$	$^3F_4$	48.647	
11	$3d^94p$	$^1D_2$	48.759	
12	$3d^94p$	$^1P_1$	48.809	48.817
13	$3d^94p$	$^3D_3$	48.866	
14	$3d^94p$	$^3P_0$	49.518	
15	$3d^94p$	$^3F_3$	49.728	
16	$3d^94p$	$^3D_1$	49.742	49.726
17	$3d^94p$	$^3D_2$	49.848	
18	$3d^94d$	$^3S_1$	54.765	
19	$3d^94d$	$^3G_4$	54.982	
20	$3d^94d$	$^3D_2$	55.036	
21	$3d^94d$	$^1F_3$	55.127	
22	$3d^94d$	$^1P_1$	55.188	
23	$3d^94d$	$^3G_5$	55.210	
24	$3d^94d$	$^3D_3$	55.375	
25	$3d^94d$	$^1D_2$	55.423	
26	$3d^94d$	$^3F_4$	55.446	
27	$3d^94d$	$^3P_0$	55.633	
28	$3d^94d$	$^3D_1$	55.962	
29	$3d^94d$	$^3G_3$	55.979	
30	$3d^94d$	$^3P_1$	56.192	
31	$3d^94d$	$^3F_2$	56.218	
32	$3d^94d$	$^1G_4$	56.297	
33	$3d^94d$	$^3P_2$	56.373	
34	$3d^94d$	$^3F_3$	56.449	
35	$3d^94d$	$^1S_0$	57.954[c]	
36	$3d^94f$	$^3P_0$	61.604	
37	$3d^94f$	$^3P_1$	61.689	
38	$3d^94f$	$^3P_2$	61.823	
39	$3d^94f$	$^3H_6$	61.869	
40	$3d^94f$	$^3H_5$	61.880	
41	$3d^94f$	$^1D_2$	61.988	
42	$3d^94f$	$^3F_3$	62.004	
43	$3d^94f$	$^1G_4$	62.060	
44	$3d^94f$	$^3F_4$	62.093	
45	$3d^94f$	$^3G_5$	62.137	
46	$3d^94f$	$^1F_3$	62.177	
47	$3d^94f$	$^3D_1$	62.373	62.339
48	$3d^94f$	$^3D_2$	62.839	
49	$3d^94f$	$^3H_4$	62.889	
50	$3d^94f$	$^1H_5$	62.979	

Table 1. (continued.)

Index	Configuration	Symmetry	MCDF[a]	Observed[b]
51	$3d^9 4f$	$^3F_2$	63.006	
52	$3d^9 4f$	$^3D_3$	63.093	
53	$3d^9 4f$	$^3G_4$	63.157	
54	$3d^9 4f$	$^3G_3$	63.167	
55	$3d^9 4f$	$^1P_1$	64.133	63.962

[a] This work (no Breit-plus-QED).
[b] Wyart *et al* (1985).
[c] Lowered by 0.56 Ry—see text for discussion.

opacity. Photon related processes require the dipole matrix file RECUPD.DAT as well. In figure 1 we show a flow diagram of the relationship and interconnectivity between the code suites just discussed. Only the serial, undamped, versions of each stage are shown.

The outer-region solutions neglect the small component of the wavefunction, which is valid here (Norrington and Grant 1987) as it is the residual charge which is the relevant quantity ($z = 26$ for Ni-like Xe). Of particular relevance, we note that our STGF suite of codes (serial & parallel and damped & undamped) can also take the R-matrix boundary solution from a full DARC inner-region calculation. This was part of our testing procedure during the development of DTO3. We also note that serial & parallel and damped & undamped aside, our single STGF interfaces transparently with all standard inner region R-matrix packages.

3. Structure

We include the 129 levels arising from the configurations $3d^{10}$ and $3d^9 nl$ for $n = 4, 5$ and $l = 0$ to $n - 1$ in Xe^{26+}. MCDF energy levels were calculated with GRASP^0 in extended-average-level mode. Results from utilizing just the Dirac–Coulomb Hamiltonian are presented in table 1 for the lowest 55 levels. The inclusion of Breit plus QED contributions tends to lower the upper levels by up to 0.04 Ry; however, they are not present in the atomic structure generated by DARC.

There is a paucity of observed data for comparison. Wyart *et al* (1985) observed seven lines from $3d^9 n = 4$ to the ground. Skobelev *et al* (1999) observed three of the same lines as Wyart *et al* (1985)—those from $3d^9 4p$ which are dipole-connected to the ground. Skobelev *et al* (1999) also carried out extensive theoretical calculations, including MCDF, but only reported results for those levels which are dipole-connected to the ground.

Wyart (1987) has carried out Slater–Condon-type calculations for the $3d^9 4s$, 4p and 4d levels of Ru^{16+} through Sn^{22+} based on fitting the Z-expansion coefficients to observed energies for the $3d^9 4s$ and 4p levels in Mo^{14+}. We have carried out similar structure calculations for Mo^{14+} and Ag^{19+}. Based upon the comparison of the resultant energy levels with those of Wyart (1987), we have lowered our ground-state energy of Xe^{26+} by 0.1 Ry.

Interest in the x-ray lasing transition $3d^9 4d^1 S_0 \rightarrow 3d^9 4p^1 P_1$ in Ni-like ions means that an accurate separation for these two levels is known (see Li *et al* (1998)). As noted by Wyart (1987), the *ab initio* predicted position of the upper level is too high. We have lowered this upper level by 0.56 Ry so as to match the separation reported by Li *et al* (1998).

4. Collisions

4.1. Calculations

We carried out a 129CC Dirac–Coulomb R-matrix calculation using the code set-up described in section 2. This resulted in a maximum of 821 channels. We used 21 continuum basis
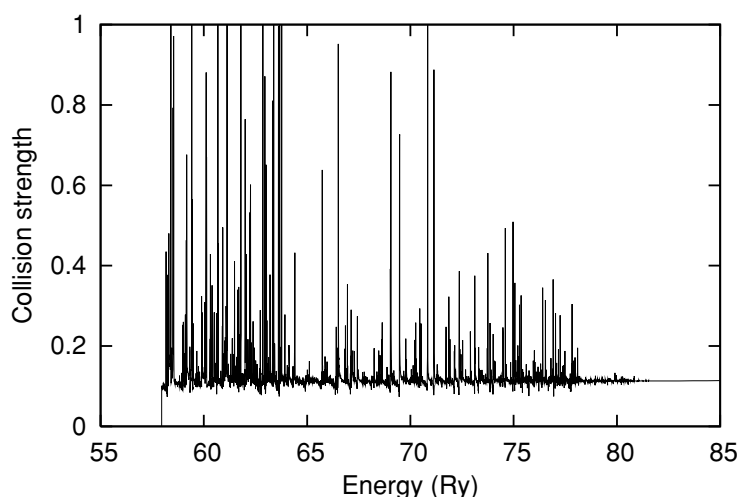
Figure 2. 129CC Dirac–Coulomb R-matrix collision strength for the $3d^{10}\,^1S_0$–$4d\,^1S_0$ transition in Xe^{26+}.

orbitals for $2J = 1$–43 and 16 orbitals for $2J = 45$–71. This resulted in a maximum $(N+1)$-electron Hamiltonian rank of 17 356 and 13 136, respectively. The contribution from $2J > 71$ ('top-up') was obtained for dipole transitions using the powerful sum rule due to Burgess (1974)[4] and for non-dipole transitions by assuming a geometric series in energy, taking care to switch over smoothly to the degenerate energy-limiting case (Burgess *et al* 1970). We used an energy mesh of $1 \times 10^{-5}z^2$ Ry through the resonance region (for $2J = 1$–23), which resulted in 5680 points, and a mesh of $1 \times 10^{-3}z^2$ Ry at higher energies and J. Collision strengths were calculated up to 350 Ry and then convoluted with a Maxwellian distribution to form effective collision strengths for all 8256 inelastic transitions. These were tabulated over 10^5–10^8 K in the ADAS *adf04* format along with the target energy levels and dipole radiative rates. These rates were determined consistently with and from the collision calculation by de-coupling the core from the $(N + 1)$-electron long-range dipole coupling potential.

4.2. Results

In figure 2 we present the results of our 129CC level Dirac–Coulomb R-matrix calculation for the strong $J = 0$–0 collision strength for the $3d^{10}\,^1S_0$–$3d^9 4d\,^1S_0$ transition in Xe^{26+}, which populates the upper level of the lasing transition $3d^9 4d\,^1S_0 \rightarrow 3d^9 4p\,^1P_1$. In figure 3 we compare the Maxwellian-averaged effective collision strength (upsilon) for this transition against that from baseline plane-wave Born data. There is about an 18% increase at $\log T(K) = 6.8$, which corresponds to the temperature of peak fractional abundance for Xe^{26+} over a wide range of electron densities.

In figure 4 we present our Dirac–Coulomb R-matrix ordinary and effective collision strengths for the three $J = 0$–1 transitions $3d^{10}$–$3d^9 4p$ in Xe^{26+}. The energy shown is that relative to the upper level for ordinary collision strengths and the corresponding temperature for the effective collision strengths, i.e. 40 Ry corresponds to $\log T(K) = 6.8$ again. For all three transitions the plane-wave Born collision strengths lie close to the R-matrix background

---

[4] We note that the STGFJJ code distributed with DARC reverts to using the slowly-convergent geometric series for dipole top-up when jj-coupling is used, i.e. with DARC (and, for that matter, when jK-coupling is used, i.e. for a Breit–Pauli R-matrix calculation).
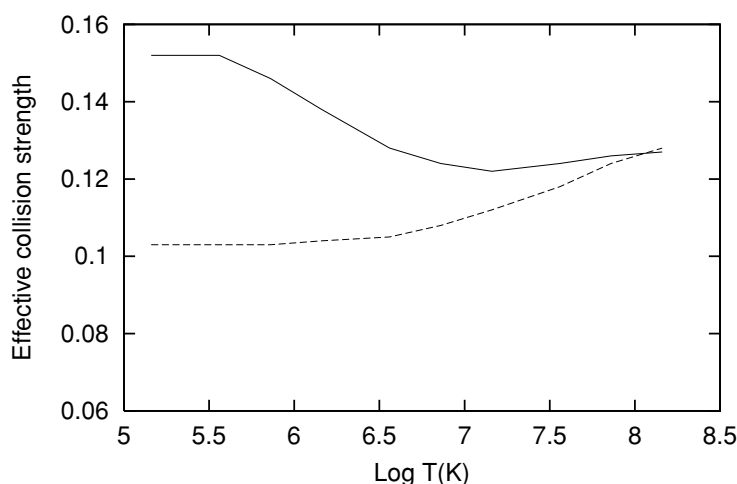
Figure 3. Effective collision strengths for the $3d^{10}$ $^1S_0$–$4d^1S_0$ transition in Xe^{26+}: solid curve, 129CC Dirac–Coulomb R-matrix; dashed curve, plane-wave Born (baseline data).

collision strengths. The rise of the R-matrix effective collision strength curve is indicative of the strength of the resonant enhancement, which is roughly a factor of 2 at 40 Ry.

In figure 5 we present similar results for the three $J = 0$–1 transitions $3d^{10}$–$3d^9 4f$. We note that there is a much wider range of strengths, in contrast to $3d^{10}$–$3d^9 4p$, with excitation to the highest level being particularly strong. The comparison of plane-wave Born collision strengths with (background) R-matrix collision strengths is also quite different from the case of $3d^{10}$–$3d^9 4p$. The plane-wave Born collision strength is an order of magnitude weaker than the R-matrix one for the 1–37 transition. For the 1–47 and 1–55 transitions, the plane-wave Born collision strength lies above the R-matrix effective collision strength, even with the moderate resonant enhancement of the latter for the 1–47 transition.

5. Modelling

5.1. Emissivity

The total emissivity in the line $j \rightarrow k$ is defined by

$$\varepsilon^z_{j \rightarrow k} \equiv N^z_j A^r_{j \rightarrow k}, \tag{1}$$

where N^z_j is the population of the upper level j of the ionization stage z and $A^r_{j \rightarrow k}$ is the radiative transition rate for the $j \rightarrow k$ line.

5.1.1. Photon emissivity coefficient. In the GCR picture (Summers 1994, Summers *et al* 2002) the excited-state level (denoted by Roman indices) populations, N^z_j, are assumed to be in quasi-static equilibrium with respect to the dominant metastable level (denoted by Greek indices) populations. Thus,

$$N^z_j = \sum_\sigma N_e {}^X\mathcal{F}^z_{j\sigma} N^z_\sigma, \tag{2}$$

where ${}^X\mathcal{F}^z_{j\sigma}$ is the effective excitation contribution to the population of j from σ. (In general there are also contributions from recombination and ionization, from stages $z + 1$ and $z - 1$, respectively.) The corresponding metastable-resolved photon emissivity coefficient is defined by
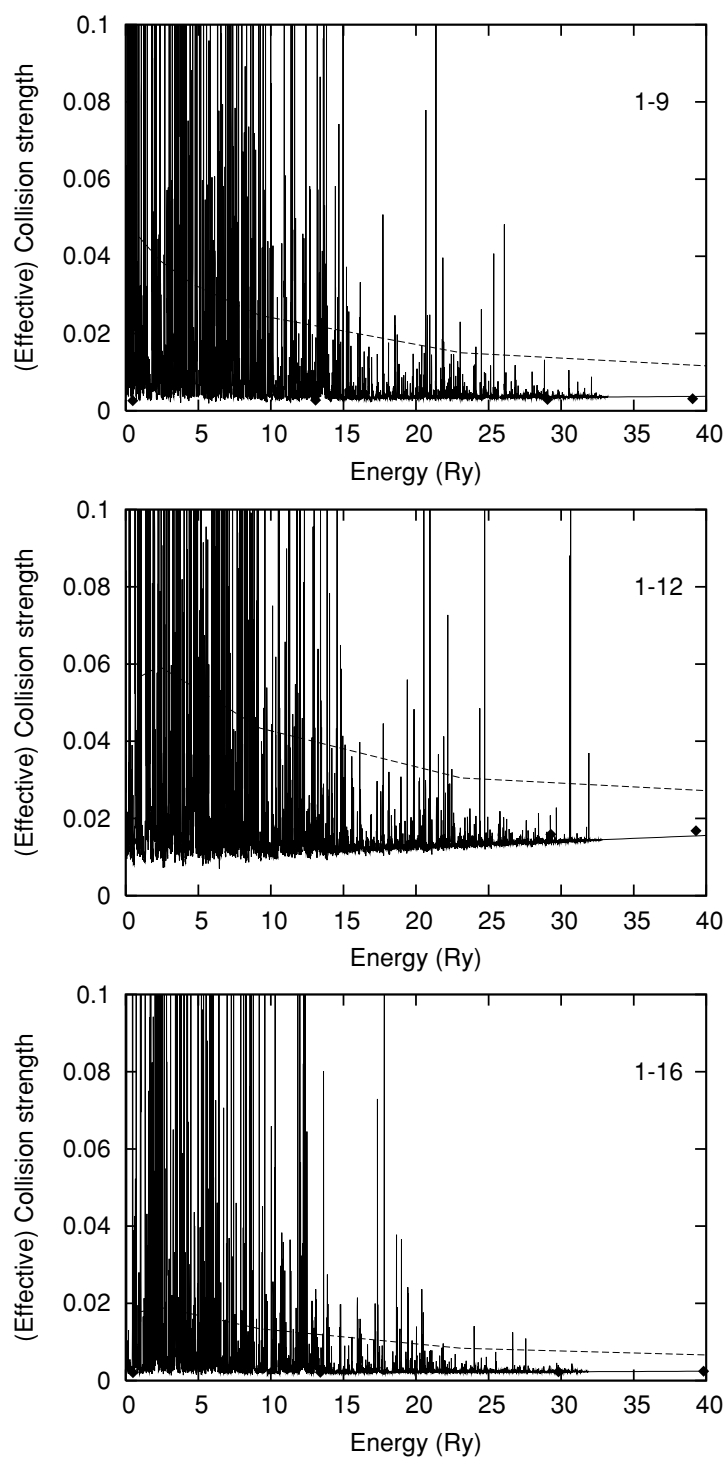
Figure 4. Results for the three $J = 0$–1 transitions $3d^{10}$–$3d^9 4p$ in Xe^{26+}. Solid and dashed lines, 129CC Dirac–Coulomb R-matrix ordinary and effective collision strengths, respectively; diamonds, plane-wave Born collision strengths.
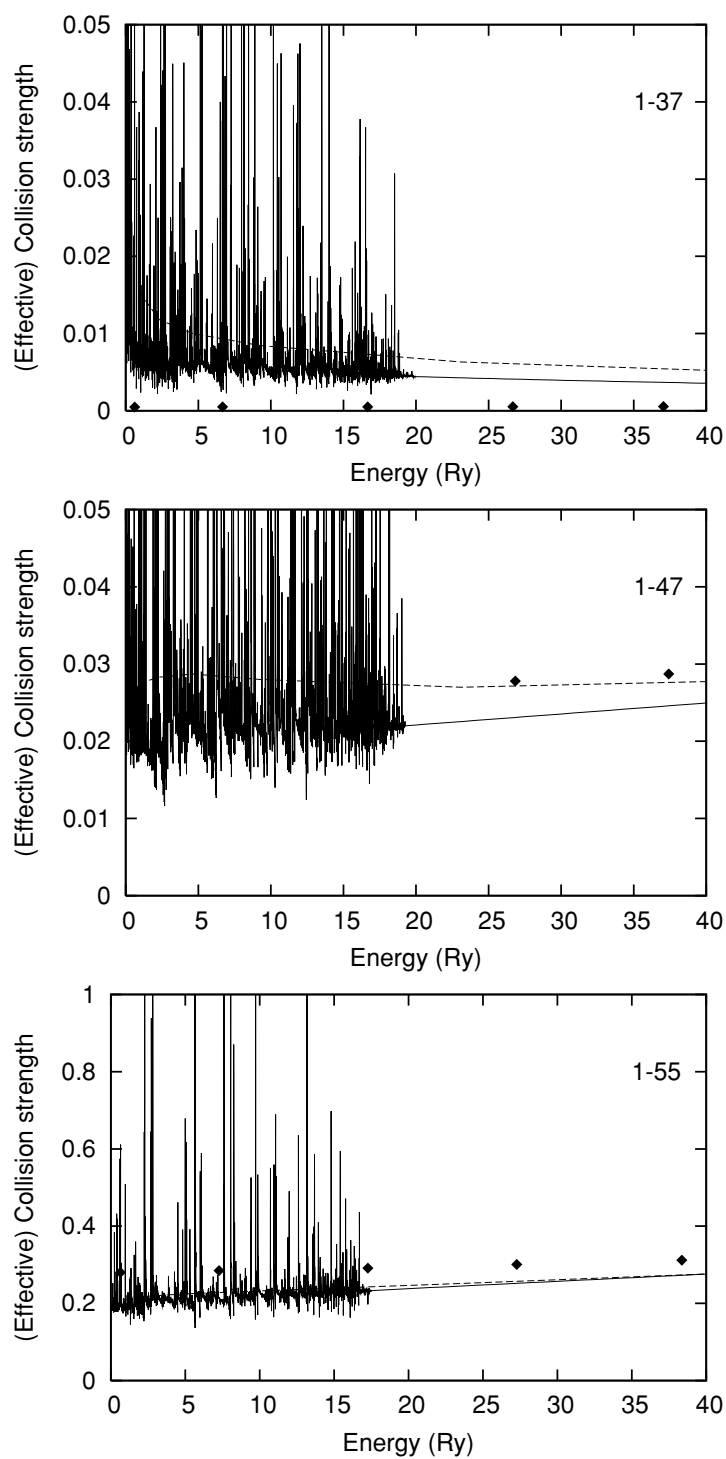
Figure 5. Results for the three $J = 0$–1 transitions $3d^{10}$–$3d^9 4f$ in Xe^{26+}. Solid and dashed lines, 129CC Dirac–Coulomb R-matrix ordinary and effective collision strengths, respectively; diamonds, plane-wave Born collision strengths.

$$^{\mathrm{X}}\mathcal{PEC}_{\sigma, j \to k}^{z} \equiv {}^{\mathrm{X}}\mathcal{F}_{j\sigma}^{z} A_{j \to k}^{\mathrm{r}}. \tag{3}$$

Thus, the contribution to the emissivity from excitation is given by

$$^{\mathrm{X}}\varepsilon_{j \to k}^{z} = N_{\mathrm{e}} \sum_{\sigma} {}^{\mathrm{X}}\mathcal{PEC}_{\sigma, j \to k}^{z} N_{\sigma}^{z}. \tag{4}$$

Note that in the low-density limit

$$^{\mathrm{X}}\mathcal{F}_{j\sigma}^{z} \sum_{k<j} A_{j \to k}^{\mathrm{r}} = q_{\sigma \to j}^{z}, \tag{5}$$

where $q_{\sigma \to j}^{z}$ is the electron-impact excitation rate coefficient from the σth metastable (which may include a cascade correction factor). So (on dropping the x label)

$$\mathcal{PEC}_{\sigma, j \to k}^{z} = \frac{q_{\sigma \to j}^{z} A_{j \to k}^{\mathrm{r}}}{\sum_{i<j} A_{j \to i}^{\mathrm{r}}}. \tag{6}$$

5.1.2. Feature photon-emissivity coefficient. Heavy species give rise to too many transitions to be described usefully by individual line emissivities. Instead, we consider an envelope of lines, defined on a wavelength interval, which is a composite feature of many individual lines. This leads in turn to a feature photon-emissivity coefficient ($\mathcal{F}$-$\mathcal{PEC}$) as follows: define a spectral interval $[\Lambda_0, \Lambda_1]$ which is subdivided into I_{p} intervals

$$\lambda_i^{[0,1]} = \left[\Lambda_0 + i \frac{\Lambda_1 - \Lambda_0}{I_{\mathrm{p}}}, \Lambda_0 + (i+1) \frac{\Lambda_1 - \Lambda_0}{I_{\mathrm{p}}} \right] \tag{7}$$

for $i = 0, \dots, I_{\mathrm{p}} - 1$.

Next, let $\phi_{j \to k}(\lambda)$ be the normalized emission line profile. Then, the envelope-feature photon-emissivity coefficient vector is defined by

$$\mathcal{F}\text{-}\mathcal{PEC}_{\sigma, i}^{z, [0,1]} \equiv \sum_{j \to k} \mathcal{PEC}_{\sigma, j \to k}^{z} \int_{\lambda_i^0}^{\lambda_i^1} \phi_{j \to k}(\lambda) \, \mathrm{d}\lambda. \tag{8}$$

We adopt a default broadening which is Doppler at the electron temperature. Further (e.g. instrumental) broadening can be easily introduced retrospectively on top of this minimal broadening.

5.1.3. Stage-composite feature. To model meaningfully a feature composed of contributions from more than one ionization stage, we introduce a generalized contribution function, $\mathcal{GTN}_{j \to k}$, which is defined in terms of equilibrium ionization fractional abundances $\left. \left(N_{\sigma}^{z} / N_{\mathrm{tot}} \right) \right|_{\mathrm{eq}}$ by (for excitation)

$$\mathcal{GTN}_{j \to k} \equiv \sum_{\sigma} \mathcal{PEC}_{\sigma, j \to k}^{z} \left. \frac{N_{\sigma}^{z}}{N_{\mathrm{tot}}} \right|_{\mathrm{eq}}, \tag{9}$$

where there again exist also contributions from ionization and recombination, in general. $\mathcal{GTN}$ is similar to the $\mathcal{G}(T_{\mathrm{e}})$ function used in solar astrophysics (omitting the $N_{\mathrm{H}}/N_{\mathrm{e}}$ ratio) but it depends on density as well and is more suited to general plasma analysis.

Analogously, in the spectral interval $[\Lambda_0, \Lambda_1]$, we define the envelope-feature generalized contribution function vector by

$$\mathcal{F}\text{-}\mathcal{GTN}_i^{[0,1]} \equiv \sum_{j \to k} \mathcal{GTN}_{j \to k} \int_{\lambda_i^0}^{\lambda_i^1} \phi_{j \to k}(\lambda) \, \mathrm{d}\lambda \tag{10}$$

$$= \sum_{\sigma} \mathcal{F}\text{-}\mathcal{PEC}_{\sigma, i}^{z, [0,1]} \left. \frac{N_{\sigma}^{z}}{N_{\mathrm{tot}}} \right|_{\mathrm{eq}}. \tag{11}$$
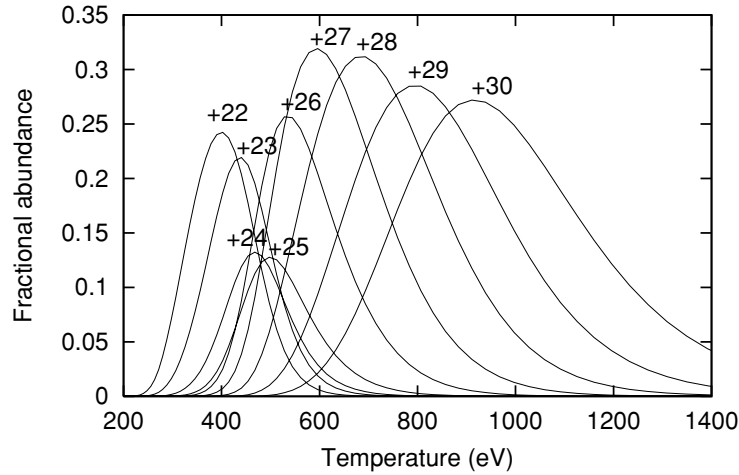
Figure 6. Fractional abundance curves for Xe^{q+} for $q = 22$–30 at $N_e = 10^{13}$ cm^{-3}.

5.1.4. Baseline ionization balance. The full metastable-resolved GCR ionization balance used for light species is overkill for heavy species at this point in time. Rather, we make use of the Case B⁵ baseline approach to ionization balance (Summers 2003). Here, the total effective ionization rate coefficient is taken to be that from the ground state and it includes contributions from both direct plus excitation–autoionization. It is a parametrization based upon the semi-empirical formulae of Burgess and Chidichimo (1983), together with shell strategies stemming from Summers and Hooper (1983). The Lotz (1968) formula takes account of direct ionization only. The total effective recombination rate coefficient is taken to be the sum of ground-state partial radiative and dielectronic recombination rate contributions which is truncated at the density dependent *n*-cut-off due to Wilson (1962). Radiative recombination is taken to be hydrogenic but described by effective principal quantum numbers ν and with fractional recombination into the lowest *n*-shell. There are further parametrization adjustments which were obtained from fits to higher precision data. Dielectronic recombination into final *nl*-subshells is determined via the Burgess–Bethe general program (BBGP)—see Badnell *et al* (2003) for a detailed exposition. Allowance is made for the energetically *n*-dependent opening-up of dielectronic capture and alternative Auger channels together with precise energies for low-lying resonances which strongly affect low temperature recombination. None of these issues are addressed by the Burgess general formula (Burgess 1965).

5.2. Results

In figure 6 we show the stage-resolved Case B baseline ionization balance for Xe, centred upon Xe²⁶⁺, obtained at $N_e = 10^{13}$ cm^{-3}. An electron density of $N_e = 10^{13}$ cm^{-3} is relevant for ITER, but in fact there is not too much change in the picture over the range $N_e = 10^8$–10^{14} cm^{-3}, particularly on excluding Xe²⁴⁺ and Xe²⁵⁺, which have small abundances.

In figure 7 we show the $\mathcal{F}$-$\mathcal{GTN}$ (equal to $(N_\sigma^z/N_{tot})|_{eq}\mathcal{F}$-$\mathcal{PEC}^z$) for Xe in the wavelength range 10–20 Å with $I_p = 102.4$, obtained at the temperature of peak fractional abundance for Xe²⁶⁺ ($T_e = 550$ eV) at $N_e = 10^{13}$ cm^{-3}. Apart from the small feature below 18 Å,

---

⁵ Case A baseline ionization balance utilizes the general formulae of Burgess (1965) and Lotz (1968) for the total dielectronic recombination and ionization rate coefficients, respectively.
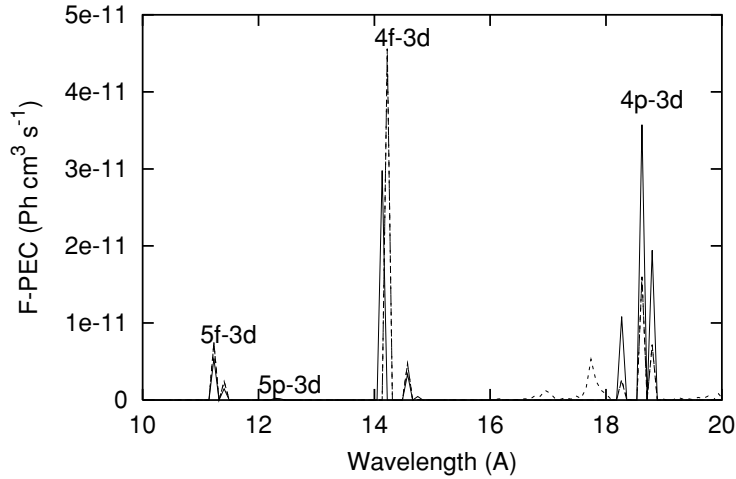
Figure 7. $\mathcal{F}\text{-}\mathcal{GTN} = (N^z/N_{\text{tot}})|_{\text{eq}}\mathcal{F}\text{-}\mathcal{PEC}^z$ for Xe^{q+} at $T_e = 550$ eV and $N_e = 10^{13}$ cm^{-3}: solid curve, utilizing Dirac–Coulomb R-matrix excitation data; dashed curve, utilizing plane-wave Born (baseline) excitation data; both for Xe^{26+} only. The dotted curve denotes features arising from other Xe ionization stages.

all features are for Xe^{26+}. The most prominent feature (4f $\rightarrow$ 3d) has been observed by Ditmire *et al* (1998) following irradiation of a target of Xe clusters by 10^{17} W cm^{-2} picosecond laser pulses. There are three $J = 1 \rightarrow 0$ transitions, at 14.8, 14.6 and 14.2 Å. There are also three $J = 1 \rightarrow 0$ transitions in the 4p $\rightarrow$ 3d feature between 18 and 19 Å. The pattern is repeated at shorter wavelengths for $n = 5$, although the 5p $\rightarrow$ 3d feature is barely visible at around 12.4 Å.

On comparing the baseline plane-wave Born results for Xe^{26+} against those obtained on using our Dirac–Coulomb R-matrix collision data, we see that the plane-wave Born results give a reasonable qualitative description of the spectral signature but, quantitatively, the R-matrix generated $\mathcal{F}\text{-}\mathcal{PEC}$s are about a factor of 2 greater for the 4p $-$ 3d feature, while the dominant 4f $-$ 3d feature is about two thirds of the Born. These differences are a direct reflection of the differences in the effective collision strengths which populate the upper level in each case—see section 4.2.

Finally, the $\mathcal{F}\text{-}\mathcal{PEC}$s change little with density until $N_e \gtrsim 10^{16}$ cm^{-3} when collisional redistribution starts to take effect.

6. Summary

We have interfaced the set-up of the $(N+1)$-electron Dirac–Coulomb Hamiltonian from DARC with our parallel diagonalization and outer-region R-matrix codes. We have used this new code suite to carry out a 129CC level R-matrix calculation for the electron-impact excitation of Xe^{26+} and have archived effective collision strengths for all 8256 inelastic transitions, along with dipole radiative rates and energy levels, in the ADAS *adf04* file format. We have utilized this data to generate the spectral signature of Xe^{26+} in terms of feature photon-emissivity coefficients ($\mathcal{F}\text{-}\mathcal{PEC}$s) at an ITER relevant density of $N_e = 10^{13}$ cm^{-3}. We have compared the $\mathcal{F}\text{-}\mathcal{PEC}$s which arise from using the Dirac–Coulomb R-matrix excitation data with those obtained using semi-relativistic plane-wave Born excitation data, which forms the heavy species baseline excitation data within ADAS. The plane-wave Born results give a reasonable

qualitative description of the spectral signature but differ quantitatively by up to a factor of two from the R-matrix generated $\mathcal{F}$-$\mathcal{PEC}$s. The baseline approach (including plane-wave Born excitation data) utilizing feature photon-emissivity coefficients is readily applicable to describing the spectral signature of the extended range of complex heavy species which are likely to arise in fusion diagnostics for ITER.

Acknowledgments

References

Ait-Tahar S, Grant I P and Norrington P H 1996 *Phys. Rev.* A **54** 3984–9
Badnell N R 1987 *J. Phys. B: At. Mol. Phys.* **19** 3827–35
Badnell N R 1997 *J. Phys. B: At. Mol. Opt. Phys.* **30** 1–11
Badnell N R, O'Mullane M G, Summers H P, Altun Z, Bautista M A, Colgan J, Gorczyca T W, Mitnik D M, Pindzola M S and Zatsarinny O 2003 *Astron. Astrophys.* **409** 1151–65
Ballance C P and Griffin D C 2004 *J. Phys. B: At. Mol. Opt. Phys.* **37** 2943–57
Berrington K A, Burke P G, Butler K, Seaton M J, Storey P J, Taylor K T and Yan Y 1987 *J. Phys. B: At. Mol. Phys.* **20** 6379–97
Berrington K A, Eissner W B and Norrington P H 1995 *Comput. Phys. Commun.* **92** 290–420
Burgess A 1965 *Astrophys. J.* **141** 1588–90
Burgess A 1974 *J. Phys. B: At. Mol. Phys.* **7** L364–7
Burgess A and Chidichimo M C 1983 *Mon. Not. R. Astron. Soc.* **203** 1269–80
Burgess A, Hummer D G and Tully J A 1970 *Phil. Trans. R. Soc.* A **266** 225–79
Burke P G and Robb W D 1975 *Adv. At. Mol. Phys.* **11** 143–214
Cowan R D 1981 *The Theory of Atomic Structure and Spectra* (Berkeley, CA: University of California Press)
Ditmire T, Patel P K, Smith R A, Wark J S, Rose S J, Milathianaki D, Marjoribanks R S and Hutchinson M H R 1998 *J. Phys. B: At. Mol. Opt. Phys.* **31** 2825–31
Grant I P, McKenzie B J, Norrington P H, Mayers D F and Pyper N C 1980 *Comput. Phys. Commun.* **21** 207–31
ITER Physics Basis 1999 *Nucl. Fusion* **39** 2137–74
Li Y, Nilsen J, Dunn J, Osterheld A L, Ryabtsev A and Churilov S 1998 *Phys. Rev.* A **58** R2668(4)
Lotz W 1968 *Z. Physik* **216** 241–7
MacGowan B J, Maxon S, Hagelstein P L, Keane C J, London R A, Mathews D L, Rosen M D, Scofield J H and Whelan D A 1987 *Phys. Rev. Lett.* **59** 2157–60
Mitnik D M, Griffin D C, Ballance C P and Badnell N R 2003 *J. Phys. B: At. Mol. Opt. Phys.* **36** 717–30
Norrington P H 2004 online at http://www.am.qub.ac.uk/DARC
Norrington P H and Grant I P 1987 *J. Phys. B: At. Mol. Phys.* **20** 4869–81
Pütterich T, Neu R, Dux R, Kallenbach A, Fuchs Ch, O'Mullane M, Whiteford A, Summers H P and the ASDEX Upgrade team 2004 *Proc. of the 31st EPS Conference on Plasma Phys. (London, June–July 2004)* vol 28G (ECA) P-4.136
Robicheaux F, Gorczyca T W, Pindzola M S and Badnell N R 1995 *Phys. Rev.* A **52** 1319–33
Skobelev I Yu *et al* 1999 *J. Phys. B: At. Mol. Opt. Phys.* **32** 113–22
Smith B W 2004 (ed) *Proc. of Optical Microlithography XVII SPIE* vol 5377
Summers H P and Hooper M B 1983 *Plasma Phys.* **25** 1311–44
Summers H P 1994 *Adv. At. Mol. Phys.* **33** 275–319
Summers H P 2003 *ADAS User Manual Version 2.6* Online at http://adas.phys.strath.ac.uk/docs/idl-manual
Summers H P *et al* 2002 *Plasma Phys. Control. Fusion* **44** B323–38
Wilson R 1962 *J. Quant. Spectrosc. Radiat. Transfer* **2** 477–90
Wyart J-F 1987 *Phys. Scr.* **36** 234–9
Wyart J-F, Bauche-Arnoult C and Luc-Koenig E 1985 *Phys. Scr.* **32** 103–6